Spatial eigenanalysis of spectral/*hp* continuous Galerkin schemes and their stabilisation via DG-mimicking spectral vanishing viscosity for high Reynolds number flows

Rodrigo C. Moura [a],[*], Mansoor Aman [b], Joaquim Peiró [b], Spencer J. Sherwin [b]

[a] *Divisão de Engenharia Aeronáutica, Instituto Tecnológico de Aeronáutica (ITA), Brazil*
[b] *Aeronautics Department, Imperial College London, SW7 2AZ, United Kingdom*

A B S T R A C T

This study considers the spatial eigensolution analysis of spectral/*hp* continuous Galerkin (CG) schemes, complementing a recent work by Moura et al. (2016) [15] which addressed CG's temporal analysis. While the latter assumes periodic boundary conditions, the spatial approach presumes inflow/outflow type conditions and therefore provides insights for a different class of problems. The linear advection-diffusion problem is considered for a wide range of Péclet numbers, allowing for viscous effects at different intensities. The inviscid (linear advection) case receives particular attention owing to the manifestation of peculiar characteristics previously observed for discontinuous Galerkin (DG) schemes in the limit of strong over-upwinding. These effects are discussed in detail due to their potential to negatively affect solution quality and numerical stability of under-resolved simulations at high Reynolds numbers. The spectral vanishing viscosity (SVV) technique is subsequently considered as a natural stabilization strategy, in the context of linear advection. An optimization procedure is employed to match SVV diffusion levels to those of DG at appropriate polynomial orders. The resulting CG-SVV discretisations are tested against under-resolved computations of spatially developing vortex-dominated flows and display excellent robustness at high Reynolds numbers along with superior eddy-resolving characteristics at higher polynomial orders. This highlights the importance of appropriate stabilization techniques to improve the potential of spectral/*hp* CG methods for high-fidelity simulations of transitional and turbulent flows, including implicit LES / under-resolved DNS approaches.

1. Introduction

Assessing the dispersive and diffusive behaviour of any numerical scheme is a fundamental step towards the understanding of its accuracy and stability characteristics. This is particularly true for high-order methods, where the trade-off between low dissipation and numerical robustness is of critical importance for the usefulness of those methods [1,2]. As a result, dispersion-diffusion analyses have been conducted for different high-order schemes [3,4], and more recently for various spectral element methods [5–11]. The present work considers the spatial eigenanalysis of spectral/*hp* continuous Galerkin (CG) schemes [12] as applied to the (one-dimensional) linear advection-diffusion equation and the linear advection equation augmented with spectral vanishing viscosity (SVV), see e.g. [13,14].

---

* Corresponding author.
    E-mail address: moura@ita.br (R.C. Moura).

The spatial analysis addressed here is to be contrasted with the temporal analysis which is much more often found in the literature. While the latter assumes periodic boundary conditions, the former presumes inflow/outflow type conditions and is therefore concerned with a different class of problems. This study can be seen as a continuation of a previous work which considered CG's temporal eigenanalysis [15]. The present investigation has also been motivated by a recent spatial analysis of the discontinuous Galerkin (DG) method [16] that focused on the insights that eigenanalysis can provide for more complex applications, such as turbulence simulations. Hence, SVV is here considered as a natural stabilization strategy given its usage in CG-based eddy-resolving computations of turbulent flows [17–21]. We note that although DG's characteristics for implicit LES / under-resolved DNS have been analysed in different ways so far [22–25], studies for spectral/*hp* CG are not that often found in the literature. The current work aims at reducing this gap, given the potential CG also has in this field [26,27].

The SVV technique is essentially embodied in a modified diffusion operator that is designed to affect only higher order polynomial components, as a high-order viscosity (or hyperviscosity) would do. Note that higher order CG discretisations tend to reach negligible dissipation levels at high Reynolds numbers [15], whereby added stabilization techniques are required. However, the inviscid limit observed from the spatial analysis framework is more involved and in fact reproduces undesirable characteristics typical of DG in the limit of strong over-upwinding [16]. In particular, diffusion eigencurves feature "dissipation bubbles" at certain frequency ranges and the amount of damping affecting spurious reflected eigenmodes becomes negligible in the high Reynolds limit. As these issues have the potential to negatively affect solution quality and numerical robustness, candidate SVV operators must be able to help with those. The strategy followed here was to match SVV dissipation levels to those of (standard upwind) DG at appropriate polynomial orders. This was achieved with the aid of optimisation algorithms, as first suggested by [15], and proved to be a successful strategy in the suppression of the aforementioned issues. The advocated approach is tested in the context of vortex-dominated flows through a two-dimensional model problem that mimics spatially developing grid turbulence.

DG dissipation levels were chosen as reference for the SVV because of the reasonable balance DG is known to offer between numerical robustness and low dissipation at higher polynomial orders. Note that using a CG scheme with DG-like dissipation characteristics instead of employing DG itself is sometimes advantageous in terms of computational cost. First of all, DG is more naturally suited to hyperbolic conservation laws typical of compressible flows, even though nowadays there are DG formulations adapted for incompressible flows as well. In any case, for incompressible flow problems, CG solvers have been available for longer and rely on mature algorithms. Moreover, at low Mach numbers, solving the incompressible Navier-Stokes equations is usually less expensive than dealing with their compressible counterpart, which are more complex and involve additional flow variables. Another important point concerns the stability limit of explicit time-stepping inside high Reynolds-number boundary layers (especially turbulent ones). We note that incompressible formulations, when compared to compressible ones, accept larger time steps at near-wall regions as the flow velocity goes to zero (no-slip condition). Compressible formulations that are explicit in time, on the other hand, have to take into account the acoustic velocities within this fine-mesh region. This typically makes CG-based incompressible solvers much more inexpensive than DG-based compressible ones for wall-bounded turbulent flows at low Mach numbers.

This study is organized as follows. In Sec. 2, the spatial eigensolution analysis framework is presented and its application to CG is discussed. Sec. 3 addresses the spatial dispersion and diffusion characteristics for various discretisation orders and also discusses in detail the inviscid limit case. Sec. 4 is devoted to the design of appropriate SVV operators and describes the optimisation strategy adopted. In Sec. 5, numerical experiments are conducted to illustrate how the spatial eigenanalysis' results appear in under-resolved simulations and to demonstrate the performance of optimised SVV operators. Sec. 6 discusses dissipation at lower polynomial orders by comparison to previously proposed SVV kernel functions. In Sec. 7, our findings are summarized and concluding remarks are given.

2. CG's spatial eigenanalysis framework

The model problem considered here is the one-dimensional linear advection-diffusion equation in a semi-infinite domain,

$$\frac{\partial u}{\partial t} + a \frac{\partial u}{\partial x} = \mu \frac{\partial^2 u}{\partial x^2} \, , \text{ for } x > 0 \, , t > 0 \, , \tag{1}$$

where $a > 0$ is the advection velocity and $\mu > 0$ is the viscosity. Any solution to this linear problem can be written as a superposition of wave-like components such as

$$u \propto \exp\left[i(\kappa x - \omega t)\right] \, , \tag{2}$$

with κ and ω being the component's wavenumber and (angular) frequency, respectively. Accordingly, boundary conditions at $x = 0$ are assumed in the form

$$u_0(t) \propto \exp(-i\omega t) \, . \tag{3}$$

The analytical solution to this problem has been discussed in detail in [28], which considered solutions compatible with time-periodic boundary conditions.

Inserting Eq. (2) into Eq. (1) yields

$$-i\varpi + i\kappa = -\kappa^2/r\,, \tag{4}$$

where variables $\varpi = \omega/a$ and $r = a/\mu$ have been introduced. In general, both ϖ and κ can be complex, but the more interesting analyses are carried out assuming that one of them is real. From Eq. (4), one can define $\varpi = \varpi(\kappa)$, which is perhaps the most well known relation, but it is also possible to define $\kappa = \kappa(\varpi)$. Depending on this choice, two dispersion relations can be obtained, namely

$$\varpi = \kappa - i\kappa^2/r\,, \tag{5}$$
$$\kappa = \left(-1 + \sqrt{1 - 4i\varpi/r}\right)ir/2\,. \tag{6}$$

While the relation in Eq. (5) with κ real is the basis of temporal analyses, taking Eq. (6) with ϖ real is the practice in spatial analyses. Note that we will consider the positive root sign in Eq. (6) as it gives the relevant physical solution. The negative root sign is associated to a "viscous" wave that propagates contrary to the sign of a and is infinitely damped as μ approaches zero. In fact, this wave is simply non-existent in the case of pure advection. Moreover, this negative root solution is unbounded at $x \to \infty$ and is generally considered inadmissible in the solution of the model problem in question [28]. As this negative root solution also does not appear in the numerical results discussed in the present study, it will be disregarded in what follows.

Although the real and imaginary parts of Eq. (6) can be obtained analytically [28], these can be easily evaluated numerically from the formula above. It is also worth mentioning that the advection/diffusion characteristics of temporal waves, i.e. Eq. (2) with Eq. (5), and spatial waves, i.e. Eq. (2) with Eq. (6), are generally different. This is because, for complex-valued functions like $\varpi = \varpi(\kappa)$ and $\kappa = \kappa(\varpi)$, the difference between their real/imaginary parts does not amount to a simple swap of Cartesian axes. Some relations can nevertheless be drawn between these two, see e.g. [29].

Regarding CG's eigenanalysis, it is useful to start from the eigenvalue relation corresponding to the semi-discrete advection-diffusion problem in one dimension, which has been derived in [15] and reads

$$-i\varpi h\vec{u} = \boldsymbol{\Gamma}(\kappa h)\vec{u}\,, \tag{7}$$

where h is the (constant) mesh spacing employed and $\boldsymbol{\Gamma}$ is a square matrix of size $m(\text{CG}) = P$, which is the number of (independent) element-wise degrees of freedom, P being the polynomial order. In the temporal approach, for each real κh given, m complex values for ϖh are obtained directly through the eigenvalues of $\boldsymbol{\Gamma}$. In the spatial approach, however, obtaining complex-valued κh from a given real ϖh requires the solution of a determinant problem, such as

$$\det\left[\boldsymbol{\Gamma}(\kappa h) + i\varpi h\mathcal{I}\right] = 0\,, \tag{8}$$

in which $\mathcal{I}$ is the identity matrix of the required size. A slight restructuring of the above has been found to help with the numerical evaluation of its roots, as follows. Matrix $\boldsymbol{\Gamma} = \boldsymbol{\Gamma}(\kappa h)$ is defined in Eq. (24) of Ref. [15] as

$$\boldsymbol{\Gamma} = 2\left[\mathcal{L}_{\boldsymbol{M}}\,e^{-i\kappa h} + \mathcal{C}_{\boldsymbol{M}} + \mathcal{R}_{\boldsymbol{M}}\,e^{+i\kappa h}\right]^{-1}\left[\mathcal{L}_{\boldsymbol{X}}\,e^{-i\kappa h} + \mathcal{C}_{\boldsymbol{X}} + \mathcal{R}_{\boldsymbol{X}}\,e^{+i\kappa h}\right]\,, \tag{9}$$

where matrices $\mathcal{L}_{(\cdot)}$, $\mathcal{C}_{(\cdot)}$ and $\mathcal{R}_{(\cdot)}$ above stem either from the mass matrix $\boldsymbol{M}$ or from matrix $\boldsymbol{X}$, which incorporates advection/diffusion effects and depends on the Péclet number $\text{Pe} = ah/\mu = hr$, see [15] for details. Inserting Eq. (9) into Eq. (8) and rearranging yields a problem of the form

$$\det\left[\left(z^{-1}\mathcal{L}_{\boldsymbol{X}} + \mathcal{C}_{\boldsymbol{X}} + z\mathcal{R}_{\boldsymbol{X}}\right) + i\frac{\varpi h}{2}\left(z^{-1}\mathcal{L}_{\boldsymbol{M}} + \mathcal{C}_{\boldsymbol{M}} + z\mathcal{R}_{\boldsymbol{M}}\right)\right] = 0\,, \tag{10}$$

in which $z = \exp(i\kappa h)$. The above has been solved numerically for complex-valued z through MATLAB's function *newtzero*. No more than two roots have been found for each real ϖh, corresponding to: (i) the physical component that matches Eq. (6) for small ϖh, and (ii) a spurious component associated to unphysical reflections due to e.g. variations in mesh spacing. These results are similar to those found for DG in [30,16].

At this point, it is convenient to mention that Eq. (9) can also account for an SVV term which is introduced in the formulation as a modified diffusion operator. This is achieved by a simple adaptation in matrix $\boldsymbol{X}$, which consequently affects matrices $\mathcal{L}_{\boldsymbol{X}}$, $\mathcal{C}_{\boldsymbol{X}}$, and $\mathcal{R}_{\boldsymbol{X}}$, see Sec. 3.1 of Ref. [15] for details. This adaptation basically incorporates SVV's (normalized) kernel entries. These define the relative intensity in which SVV affects different polynomial modes (when written in a suitable hierarchical basis). While unit kernel entries recover the regular diffusion operator, typical SVV kernel entries increase from zero to one, so that higher order modes are more strongly damped. These entries are then scaled by SVV's base viscosity μ_{SVV}, from which a Péclet number $\text{Pe} = ah/\mu_{SVV}$ is also defined. The spatial eigenanalysis of linear advection with added SVV will be discussed in more detail in Sec. 4.

The root-finding algorithm employed in the solution of Eq. (10) benefits from a good guess for the root's location. Nevertheless, it is always possible to try random guesses for z until the desired solution is obtained. It is important to note

that MATLAB's function *newtzero* typically returns the physical and spurious solutions for z altogether for each given ϖh. To avoid scrambling these two solutions, it is useful to track them separately. This can be done by realising that physical and spurious solution components are expected to have opposite amplification behaviours, as will become clear in Sec. 3. Fortunately, this information is encapsulated in the absolute value of $z = \exp(i\kappa h)$, as

$$z = \exp\left[i\,\Re(\kappa h)\right]\exp\left[-\Im(\kappa h)\right] \; \therefore \; \Im(\kappa h) \gtrless 0 \Leftrightarrow |z| \lessgtr 1 \,, \tag{11}$$

where $\Re(\cdot)$ and $\Im(\cdot)$ stand for the real and imaginary parts of a complex number. Using these guidelines is useful because it bypasses the numerical difficulties of inverting the complex exponential function in order to access the imaginary component of κh. One can be sure that a physical root has been found simply by checking whether $|z| < 1$. A random guess for a physical solution can be of course $z = r_1 \exp(2\pi i r_2)$, where r_1 and r_2 are real numbers within $(0, 1]$. These same criteria can be used for a spurious root if one considers Eq. (10) with an inverted definition for z, i.e. $z = 1/\exp(i\kappa h) = \exp(-i\kappa h)$. Such sign change guarantees that the spurious root found through this strategy will have an absolute value smaller than unity. This spurious root will obviously have to be inverted subsequently if one is to store the actual spurious root of Eq. (10) for a given ϖh.

Once the (two) sequences of complex z values are obtained for the chosen range of ϖh, dispersion-diffusion curves can be generated by plotting $\Re(\kappa h)$ and $\Im(\kappa h)$ versus ϖh. However, while the latter can be readily obtained as $\Im(\kappa h) = -\ln|z|$, the former invariably requires using a (multi-valued) complex logarithm function, as $\Re(\kappa h) = -i\ln(z/|z|)$. It is therefore advisable that dispersion curves are carefully adjusted so as to avoid mistakes in complex phase estimates (usually seen as discontinuities on dispersion curves). Note that admissible corrections in $\Re(\kappa h)$ have to be a multiple of π. To verify whether any correction is in fact justifiable, it is worth checking the derivative of κh with respect to ϖh, which can be evaluated without ambiguity. This can be done by noting that

$$z = \exp(i\kappa h) \;\Rightarrow\; \frac{dz}{d(\varpi h)} = i\,\frac{d(\kappa h)}{d(\varpi h)}\,z \;\Rightarrow\; \frac{d(\kappa h)}{d(\varpi h)} = -\frac{i}{z}\frac{dz}{d(\varpi h)} \,, \tag{12}$$

where the rightmost derivative can be approximated numerically for a physical or spurious root z as

$$\frac{dz}{d(\varpi h)} \approx \frac{z|_{\varpi h+\epsilon} - z|_{\varpi h-\epsilon}}{2\epsilon} \,, \tag{13}$$

in which ϵ is a sufficiently small variation in ϖh. In particular, the real part of $d(\kappa h)/d(\varpi h)$ will indicate whether the slopes of dispersion curves have been evaluated correctly. With the above guidelines, fully continuous dispersion-diffusion curves have been obtained for physical and spurious modes. These are discussed in the following two sections.

3. Eigencurves for linear advection-diffusion

This section addresses the spatial eigencurves of the continuous Galerkin method for the linear advection-diffusion problem. The Péclet number $\mathrm{Pe} = ah/\mu$ mentioned in Sec. 2 is the main parameter to be varied. It represents the ratio between advective and diffusive effects and can be thought of as a local Reynolds number based on the mesh spacing h. As the eigencurves considered are defined uniquely by P and Pe, it is useful to follow [15] and work instead with the equivalent pair of variables P and $\mathrm{Pe}^* = a\hbar/\mu$, the latter being the Péclet number based on a DOF length scale ($\hbar = h/m(\mathrm{CG}) = h/P$). This will allow for a fair comparison between eigencurves with usual DOF-based normalization.

To begin with, case $\mathrm{Pe}^* = 10$ can be considered, as it represents an intermediate Péclet number such that neither advective or diffusive effects alone dominate the character of the problem [15]. Fig. 1 shows the corresponding dispersion and diffusion curves for $P = 1, \ldots, 5$, with physical modes shown in blue and spurious ones in red. The latter typically exhibit negative values for $\Re(\kappa h)$ and $\Im(\kappa h)$, meaning that spurious reflected modes are damped as they propagate backwards, i.e. contrary to the advection velocity sign. We remark that spurious reflected modes are also observed in DG's spatial eigenanalysis, cf. [16]. Note that, due to viscous effects, the reference results (dashed curves) are not straight lines, but are given by the real and imaginary parts of Eq. (6). Although the overall accuracy of the results (on a per DOF basis) can be seen to increase with P, this improvement is not very significant at $\mathrm{Pe}^* = 10$. Nevertheless, it is clear that the frequency range of negligible diffusion error is larger for $P = 5$ than for $P = 1$. The diffusion curve of case $P = 2$ seems to benefit from the fact that, as the eigencurve begins to leave its expected low-error frequency range (say, beyond $\varpi\hbar \approx 1.5$), it fortuitously "deviates" to the correct direction and ends up extending the frequency range of negligible diffusion error until about $\varpi\hbar \approx 2.5$, therefore surpassing what is achieved with higher orders (on a per DOF basis). This fortuitous behaviour of discretization $P = 2$ changes, however, with the Péclet number and does not hold anymore at, e.g. $\mathrm{Pe}^* = 5$ or $\mathrm{Pe}^* = 20$ (not shown). Lastly, it is worth pointing out that the overall diffusion levels of the spurious mode slowly decrease as the polynomial order is increased.

The limit of negligible viscosity is considered in Fig. 2, which shows case $\mathrm{Pe}^* = 1000$ for $P = 1, \ldots, 5$. This figure bears a striking resemblance with Fig. 4 of Ref. [16], which shows DG's linear advection eigencurves in the limit of strong overupwinding. Interestingly, this has been found to be more than a mere resemblance. In fact, these figures have been verified to match exactly upon superposition (not shown) for the real and imaginary parts of κ^*h vs. ϖh, i.e. when the normalizing
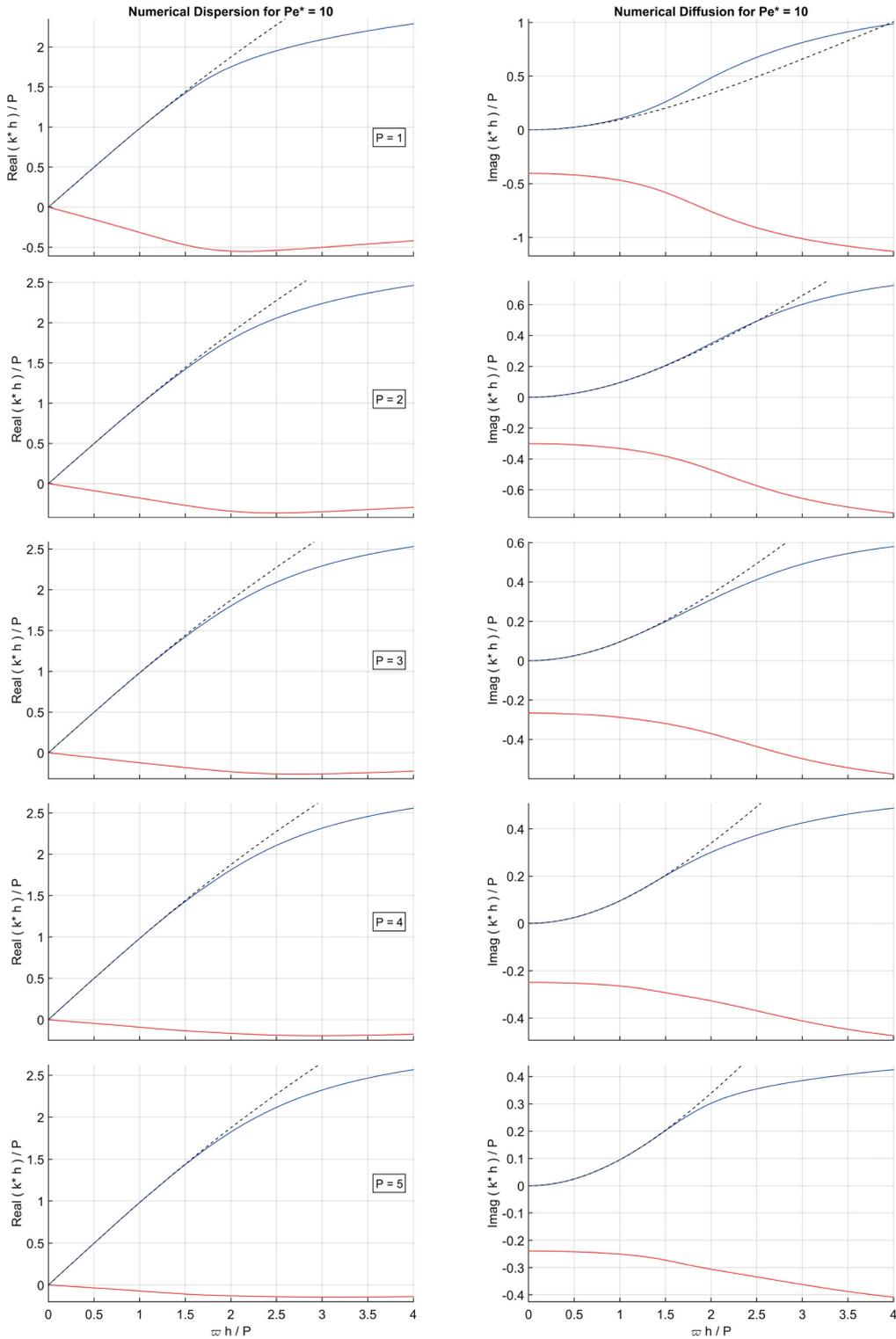
Fig. 1. Numerical dispersion (left) and diffusion (right) curves for CG-based linear advection-diffusion with Pe* = 10 and $P = 1, \ldots, 5$ (increasing from top to bottom). The dashed curves indicate the exact advection-diffusion behaviour at this Pe*. Physical (blue) and spurious (red) eigenmodes are shown. (For interpretation of the colours in the figure(s), the reader is referred to the web version of this article.)
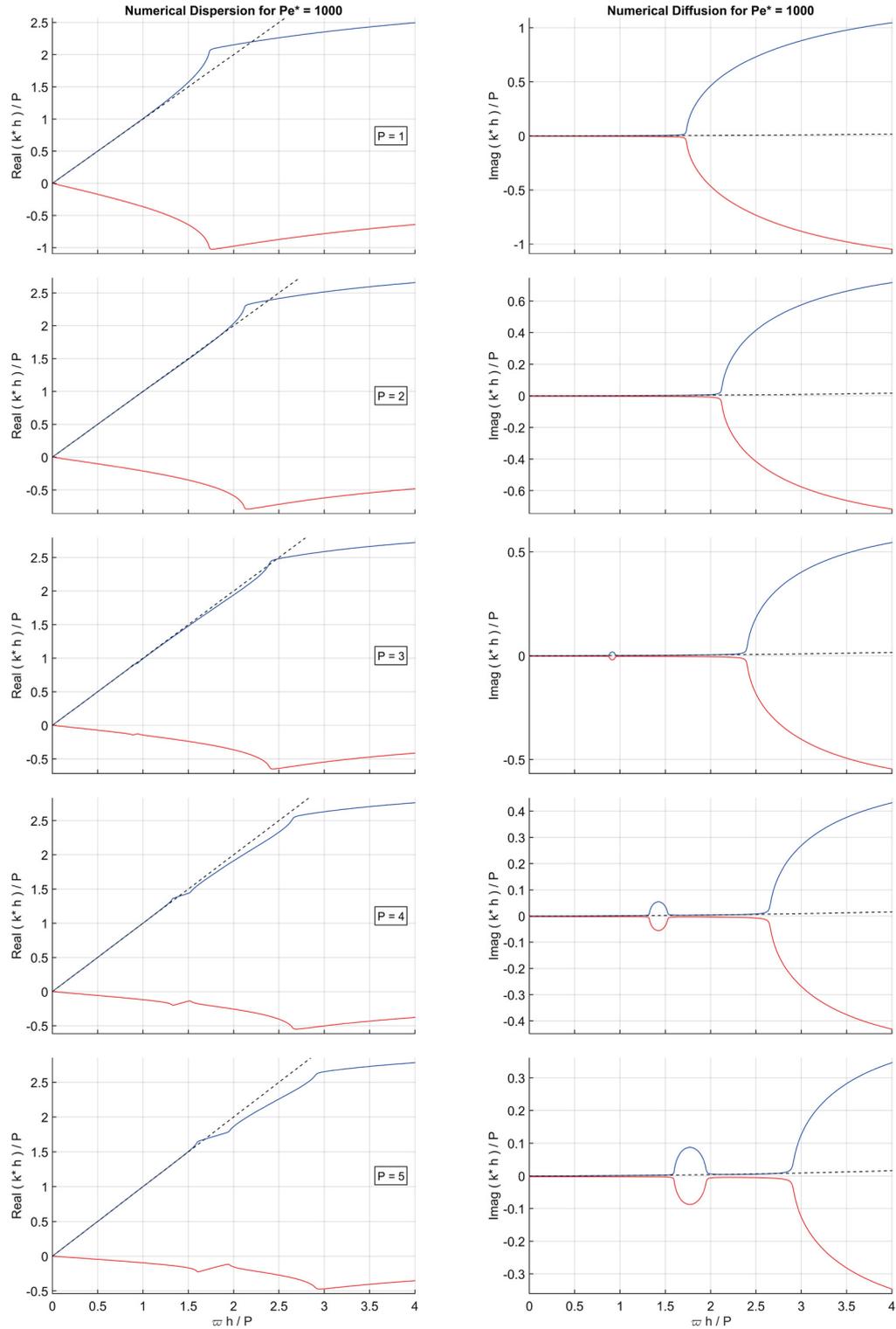
Fig. 2. Numerical dispersion (left) and diffusion (right) curves for CG-based linear advection-diffusion with Pe* = 1000 and $P = 1, \ldots, 5$ (increasing from top to bottom). The dashed curves indicate the exact advection-diffusion behaviour at this Pe*. Physical (blue) and spurious (red) eigenmodes are shown.

factors $m(\text{CG}) = P$ and $m(\text{DG}) = P + 1$ are dropped. This implies that the dispersive/dissipative behaviour of inviscid CG matches that of hyper-upwind DG for the same mesh and polynomial order − for linear advection. This equivalence of behaviours highlights that the interface continuity condition enforced in CG does not exactly correspond to a fully central finite difference-type discretization, but can introduce numerical dissipation. One should stress, however, that the inviscid CG limit is in fact similar to a dissipation-free central discretization in the setting of temporal eigenanalysis [15]. This fundamental difference highlights that spatial and temporal frameworks concern essentially different types of physical problems. For spatially developing flows, it appears that CG's $\mathcal{C}^0$ continuous interface solution is much more strongly influenced by upstream conditions (i.e. it is upwind character).

While still considering Fig. 2, note that case $P = 2$ exhibits again particularly accurate characteristics for its physical mode, with a significant frequency range of negligible numerical error. However, CG's inviscid limit, as DG's hyper-upwind limit, features spurious reflected modes subjected to very small damping. This is useful information for CG-based under-resolved turbulence computations (of spatially developing flows) at high Reynolds numbers, as it suggests that spurious reflections around regions of variable mesh spacing might interact with incoming turbulent structures, affecting solution quality and numerical robustness, as will be discussed in Sec. 5. Another feature observed in CG's inviscid limit is the presence of dissipation bubbles (for $P > 2$) that are likely to induce non-smooth dissipative features in under-resolved computations. For example, a sufficiently strong dissipation bubble might cause a "dissipative valley" in the (streamwise) energy spectrum of spatially developing turbulent flows. The effect of a dissipation bubble is illustrated next in a simple numerical example.
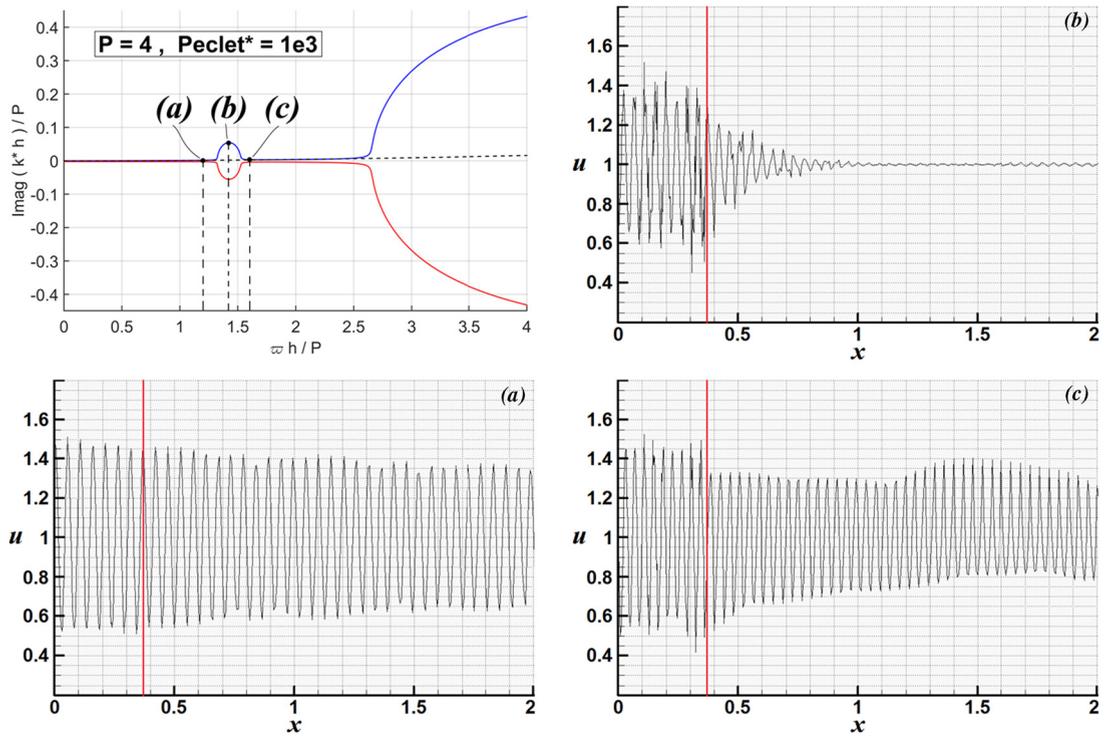
Fig. 3. Numerical experiment demonstrating the effect of dissipative bubbles for $P = 4$. Three inlet frequency values are tested, corresponding to cases (a), (b) and (c) as indicated in the top-left plot. Case (b), although of intermediate frequency, has the strongest damping factor for the transmitted wave due to the dissipative bubble. Physical (blue) and spurious (red) eigenmodes are shown in the top let graph.

A one-dimensional simulation conducted on a mesh with two grid blocks is now considered. The first block covers the initial portion of the domain ($0 \leq x \leq 0.36$) and is composed of elements of size $h_1 = 0.01$. The second block covers the remainder of the domain and consists of a coarser grid with $h_2 = 0.04$. Advection velocity and viscosity values are set to $a = 1$ and $\mu = 10^{-5}$, respectively. The polynomial order is chosen to be $P = 4$, leading to $\text{Pe}^* = 10^3$ in the second block of the domain. The relevant eigencurves for this polynomial order and Péclet number can be found in Fig. 2 and feature a dissipation bubble around $\varpi \hbar \approx 1.4$. Finally, three frequency values are considered for the boundary condition at $x = 0$, defined as $u_0 = 1 + \sin(\omega t)$. The adopted frequencies lead to $\varpi \hbar$ values of 1.2, 1.42 and 1.6, corresponding to three test cases named (a), (b) and (c), respectively. These are illustrated in Fig. 3, which shows the three cases marked on the relevant diffusion eigencurve (top-left plot) and the associated solutions after a long integration time (after transient effects). In the numerical solution, a vertical red line indicates the location after which grid spacing becomes coarser. Case (b), although of intermediate frequency, has the strongest damping factor for the transmitted wave owing to the effect of the dissipative bubble. Spurious reflections can also be seen for case (b). Note that the first mesh block features a different Péclet value

(and different $\varpi\hbar$ values) due to its finer mesh spacing. Added SVV can help to suppress dissipative bubble effects and also increases the damping of spurious modes, as will be discussed in Sec. 4.

We next consider the scenario where viscosity dominates. This high-viscosity limit is considered in Fig. 4, which shows case Pe* = 0.1 for $P = 1$ and $P = 5$. The results of intermediate order are omitted because the eigencurves change very little as P is varied. Also, eigencurves remain practically unchanged as Pe* is further reduced, indicating that the limit of viscous-dominated propagation has already been reached. Although curves in Fig. 4 might appear somewhat dull, it is important to note that both dispersion and diffusion eigencurves are practically exact regardless of the polynomial order. This indicates that, for spatially developing flows strongly dominated by viscous effects, one is essentially free to choose the polynomial order that is most efficient in one's own implementation for a given number of available DOFs.
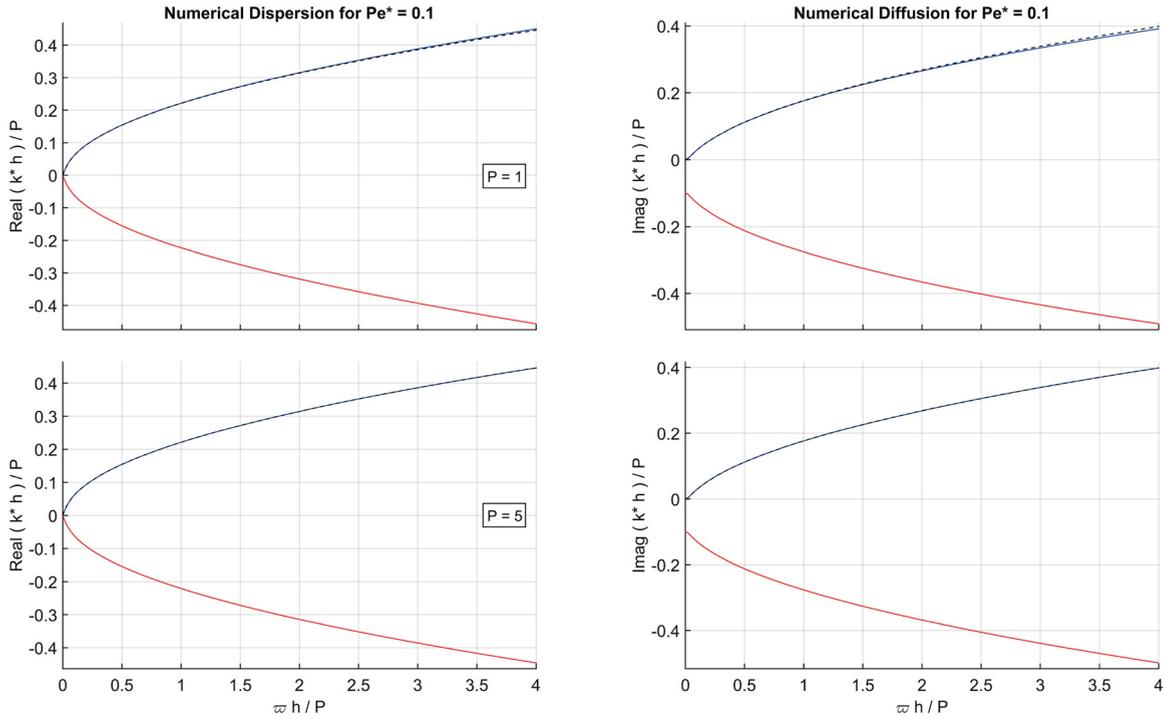
Fig. 4. Numerical dispersion (left) and diffusion (right) curves for CG-based linear advection-diffusion with Pe* = 0.1 for $P = 1$ (top) and $P = 5$ (bottom). The dashed curves indicate the exact advection-diffusion behaviour at this Pe*. Physical (blue) and spurious (red) eigenmodes are shown.

Finally, it is useful to consider how the inviscid and the high-viscosity limits are connected through intermediate Péclet numbers. Fig. 5 illustrates how the eigencurves of case $P = 2$ change as Pe* grows from 0.5 to 0.99 (top plot), then from 1.01 to 2 (centre plot) and finally from 3 to 100 (bottom plot). We note that the first (Pe* = 0.5) and last (Pe* = 100) eigencurves shown in Fig. 5 can be compared respectively to those shown in Figs. 4 and 2 for $P = 2$. The variation of the physical mode, shown in blue in Fig. 5, is somewhat straightforward. Its dispersion curves essentially bend upwards as Pe* grows. The diffusion curves initially shift upwards (top plot), then start to change this trend (centre plot) and finally bend downwards (bottom plot). On the other hand, the spurious mode, shown in red in Fig. 5, exhibits a more involved variation. Its dispersion curve starts to bend downwards at higher frequencies (top plot) and forms a steep negative slope around $\varpi\hbar \approx \sqrt{5}$ (as discussed later) as Pe* approaches unity from below. Eigencurves are generated with greater difficulty near Pe* = 1 as the roots of the associated characteristic polynomial, cf. Sec. 2, are more difficult to track. Nevertheless, soon after this "barrier", dispersion curves are found to flip upwards (centre plot) and reach positive values of $\Re(\kappa^*h)$. The abrupt slope variations shown do not result from a mistake in complex phase estimate and have been carefully verified to be correct through the strategy discussed at the end of Sec. 2. As Pe* is further increased, dispersion curves become flatter and the frequency range for which $\Re(\kappa^*h) > 0$ is enlarged, eventually reaching the origin. The diffusion curves remain always negative and form a cusp-like profile (top and centre plots) as case Pe* = 1 is approached. In the limit, the cusp reaches increasingly stronger diffusion levels (not shown) and waves of frequency around $\varpi\hbar \approx \sqrt{5}$ are infinitely damped, i.e. the spurious mode ceases to exist around this frequency. As Pe* is further increased (bottom plot), dispersion curves bend downwards and become negative again for all frequencies. The associated diffusion curves shift upwards, which indicates weaker damping of the reflected spurious mode, as expected from CG's inviscid limit.

The results obtained for $P = 2$ could have been obtained analytically as the relevant eigenmatrices, cf. Sec. 2, are of size 2×2. In particular, case Pe* = 1 can be handled without computational algebra packages due to certain symmetries of the associated characteristic polynomial. The analytical solution found for $P = 2$ and Pe* = 1 is given by
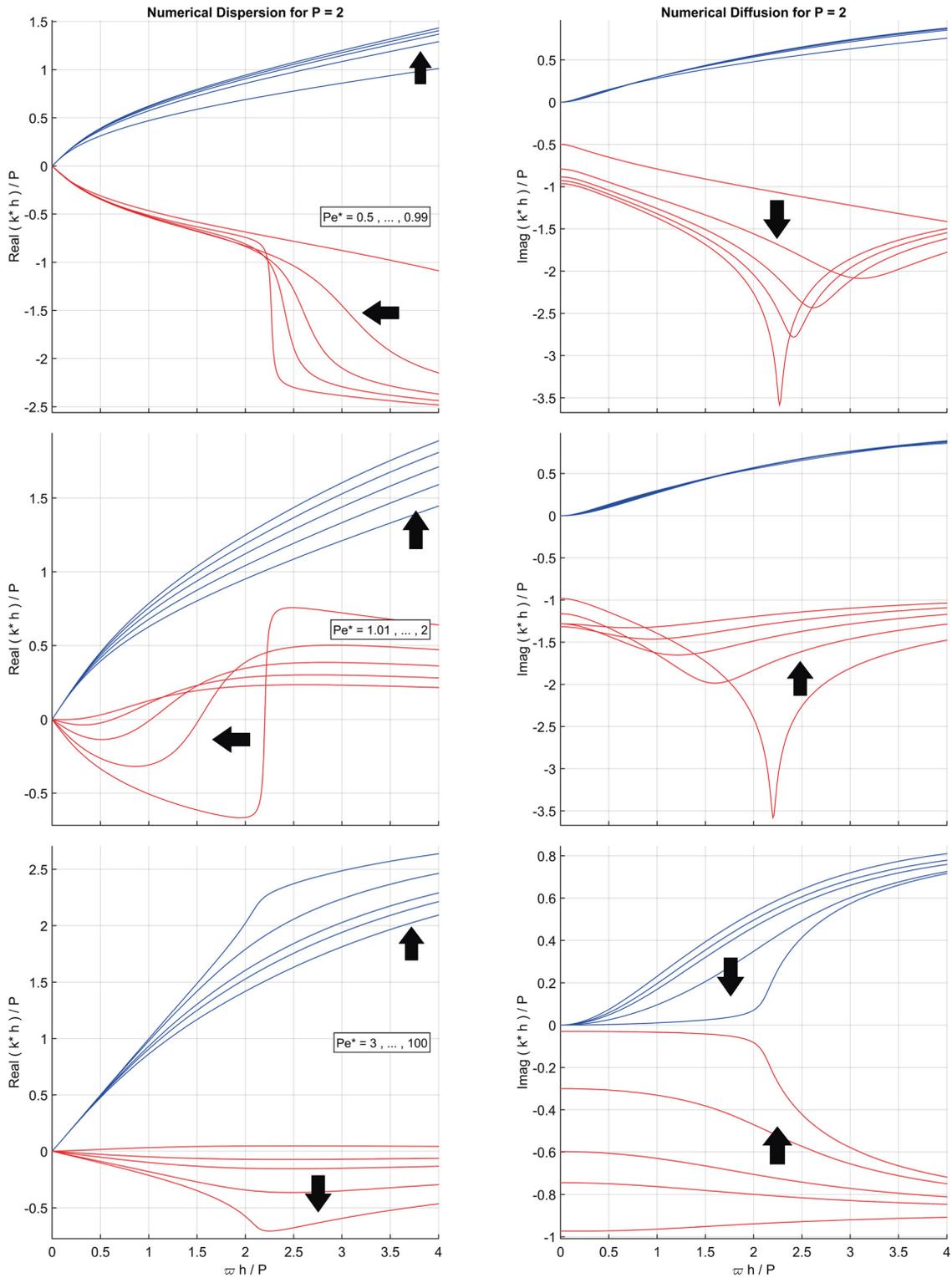
Fig. 5. Numerical dispersion (left) and diffusion (right) curves for CG-based linear advection-diffusion with $P = 2$ and Pe* varying from 0.5 to 0.99 (top), 1.01 to 2 (centre) and 3 to 100 (bottom). Arrows are used to indicate the direction of increasing Pe* for each set of curves. Physical (blue) and spurious (red) eigenmodes are shown.

$$z = \frac{3\,(\varpi h)^2 + 52i\,(\varpi h) - 80 \pm \sqrt{8\,[(\varpi h)^4 + 41i\,(\varpi h)^3 - 378\,(\varpi h)^2 - 1080i\,(\varpi h) + 450]}}{(\varpi h)^2 - 20} \,, \tag{14}$$

where $z = \exp(i\kappa h)$. The relation above makes clear that the abrupt slope variation discussed previously happens at $\varpi h = \sqrt{20}$, or equivalently, at $\varpi\hbar = \sqrt{5}$. The plots generated from this analytical solution (not shown) confirmed that the diffusion eigencurve of the spurious mode in fact tends to minus infinity at $\varpi\hbar = \sqrt{5}$, but is otherwise similar to the cusp-like profile shown in Fig. 5 for Pe* = 0.99 or Pe* = 1.01. Interestingly, the corresponding dispersion curve, although not defined at $\varpi\hbar = \sqrt{5}$, shows no abrupt slope variation and resembles an "average" between the dispersion profiles of cases Pe* = 0.99 or Pe* = 1.01, following after $\varpi\hbar = \sqrt{5}$ the trend observed from the beginning of the curve, as if there was effectively nothing special about this point.

The trends observed in Fig. 5 are not restricted to $P = 2$. In fact very similar trends have been found for $P = 4$, as shown in Fig. 6. The main difference is that the "critical" Péclet number across which dispersion curves flip from negative to positive values is Pe* ≈ 1.32, while the frequency at which this happens is $\varpi\hbar \approx 0.6$. The behaviours observed for odd polynomial orders (not shown) is similar except for the fact that dispersion eigencurves flip at the origin, instead of at a finite frequency value − this has been verified for $P = 1, 3$ and 5. For these cases, once the flip occurs, positive values of $\Re(\kappa^* h)$ will exist for all frequencies. Nevertheless, as Pe* is further increased, dispersion curves eventually change sign again. The critical Péclet numbers at which the dispersion flip takes place have been found to be, for $P = 1, 3$ and 5, respectively Pe* $\approx 2, 1.55$ and 1.46.

Despite the more involved behaviour of the dispersion curves of spurious modes, changes in $\Re(\kappa^* h)$ are somewhat inconsequential in practice. At the early stages of this study, positive $\Re(\kappa^* h)$ values for the spurious mode were thought to indicate a transmitted (instead of reflected) wave. In that case, negative $\Im(\kappa^* h)$ values for a transmitted spurious mode would mean amplification in space, i.e. a convectively unstable spurious wave. However, after some experimentation, those have not been observed in practice. It seems that spurious modes correspond always to reflected waves, the sign of $\Re(\kappa^* h)$ only affecting their phase and shape in space. This can be understood directly from Eq. (2), which can be rewritten as

$$u \propto \exp[-\Im(\kappa)\,x]\,\exp\{i\,[\Re(\kappa)\,x - \omega\,t]\}. \tag{15}$$

Note that, for example, when $\Re(\kappa^* h)$ is approximately zero (see e.g. in Fig. 5 the spurious dispersion curve of case $P = 2$ for Pe* $\gtrsim 3$), the reflected wave is expected to decay monotonically in space, oscillating only in time. Such a wave would however be strongly damped (note the large dissipation of the spurious mode at this Pe* value), making its observation difficult in practice. Therefore, positive or negative values of $\Re(\kappa^* h)$ for the spurious mode are only expected to affect its phase and its oscillatory character in space.

4. The inviscid limit and SVV stabilization

We now consider the issues encountered with CG's eigencurves in the limit of very high Péclet (or Reynolds) numbers, i.e. dissipative bubbles and the vanishing dissipation of spurious modes. The linear advection equation will be considered with SVV-based stabilization, which has the potential to suppress these issues. As in Sec. 3, the relevant set of parameters defining the eigencurves are the polynomial order P and the Péclet number, Pe* $= a\hbar/\mu_{SVV}$. (Note that we do not consider physical diffusion in this section, but only SVV. Therefore, here our Peclet number is entirely based on SVV's viscosity coefficient.) In addition, the normalized kernel entries defining the SVV operator also impact the eigencurves, as explained in Sec. 2. It is important to stress that the constant Péclet SVV approach proposed in [15] is adopted here. This approach basically prescribes that SVV's base coefficient μ_{SVV} is to be kept proportional to $a\hbar$ in order to keep SVV's reference Péclet number fixed. More specifically, one is to set $\mu_{SVV} = \mu_0 a\hbar$, so that Pe* $= \mu_0^{-1}$ is kept constant throughout the computational domain. This reference Péclet number is set to one (hence $\mu_0 = 1$) in this section, and therefore the SVV kernel entries are the only remaining parameters defining the eigencurves for each polynomial order.

The question of how much artificial viscosity is to be added in general is a difficult one because a given test case might require low diffusion levels for accuracy reasons whereas another case might be prone to instabilities and require strong stabilization. As a result, the SVV operator designed here takes the dissipation levels of DG as reference, since, among many high-order schemes, DG is arguably robust and yet weakly dissipative at higher orders. Using optimisation algorithms to match SVV's dissipation to that of DG has been explored in [15] in the context of temporal eigenanalysis. Here, an optimisation is conducted for the spatial analysis and complements the results discussed in [15]. Originally, the optimisations performed here aimed at matching DG's dissipation curves using regular plots of $\Im(\kappa^* h)$ vs. ϖh. However, consideration of these plots on a log-log scale proved to be very important. This is because the low dissipation levels observed at small ϖh would otherwise lack appropriate weight in the optimisation process. Matching these low dissipation values is critical for the accuracy of spatially developing flows involving physical instabilities and transition, as those discussed in Sec. 5. Note that non-normalised quantities are considered for the relevant plots, since there are different independent degrees of freedom in CG and DG, namely $m(\text{CG}) = P$ and $m(\text{DG}) = P + 1$.

Matching DG dissipation levels proved to be challenging due to the fact that CG's dissipative bubbles, which become much more prominent in log-log scale plots, overlap the relevant DG curves. This can be seen in Fig. 7, which shows dissipation curves for CG-based advection-diffusion (without SVV) at Pe* $= 10^{10}$ with $P = 3$ (left) and $P = 7$ (right) compared
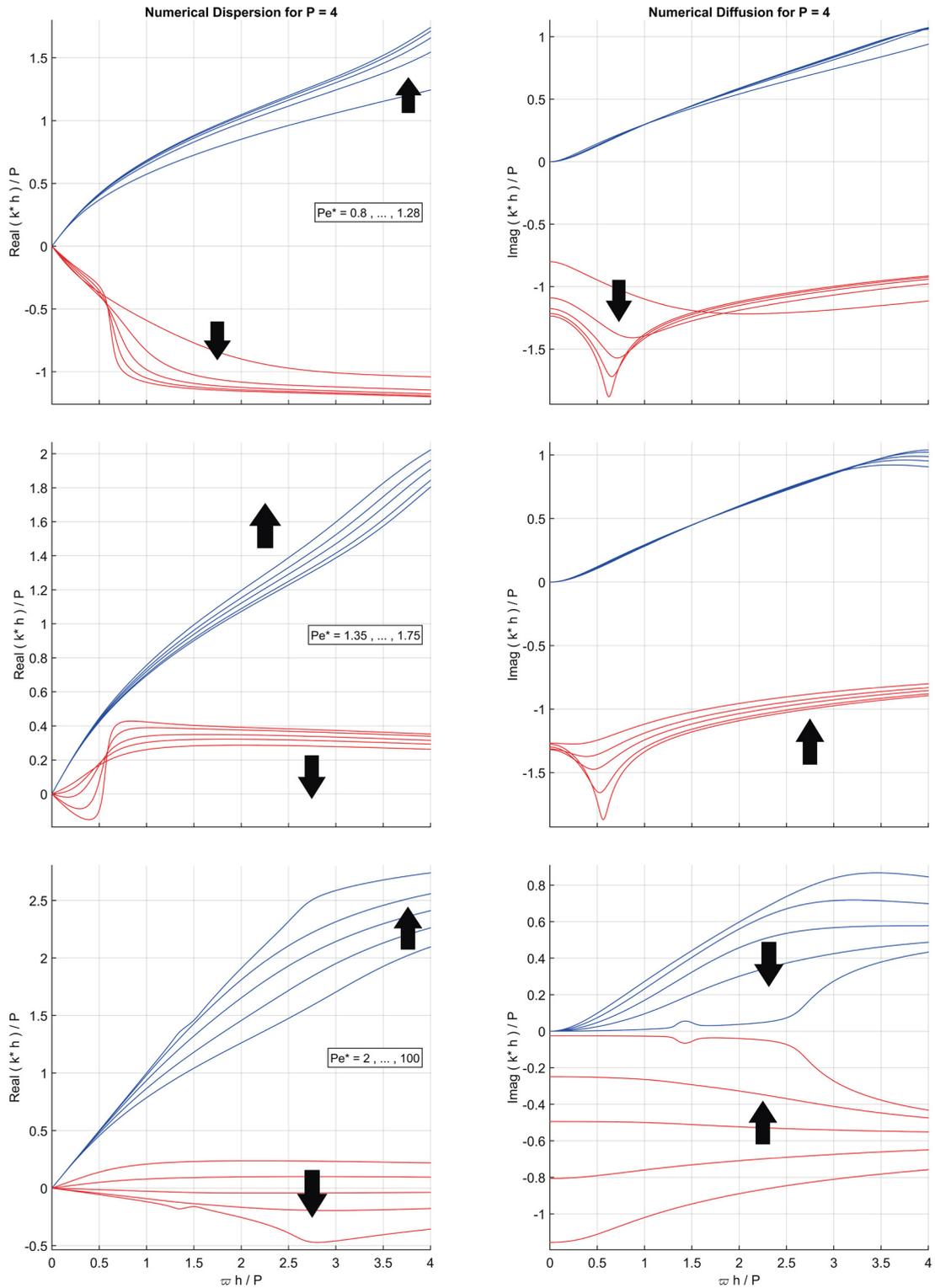
Fig. 6. Numerical dispersion (left) and diffusion (right) curves for CG-based linear advection-diffusion with $P = 4$ and Pe* varying from 0.8 to 1.28 (top), 1.35 to 1.75 (centre) and 2 to 100 (bottom). Arrows are used to indicate the direction of increasing Pe* for each set of curves. Physical (blue) and spurious (red) eigenmodes are shown.

against DG's standard upwinding dissipation curves for P, $P - 1$ and $P - 2$ (colour). As the bubbles shown do not vanish as viscosity is reduced to zero, it is clear that adding SVV will not remove them. Hence, Fig. 7 essentially demonstrates that it is not possible to match same-order dissipation curves exactly. Another difficulty arises from the fact that SVV diffusion levels obtained in the optimisation process were not steep enough to match same-order DG curves. It is possible that the slopes achieved by DG in Fig. 7, related to DG's super-convergent scaling of $\Im(\kappa^* h) \propto (\varpi h)^{2P+2}$ for small ϖh [31], are simply too steep to be matched by SVV.
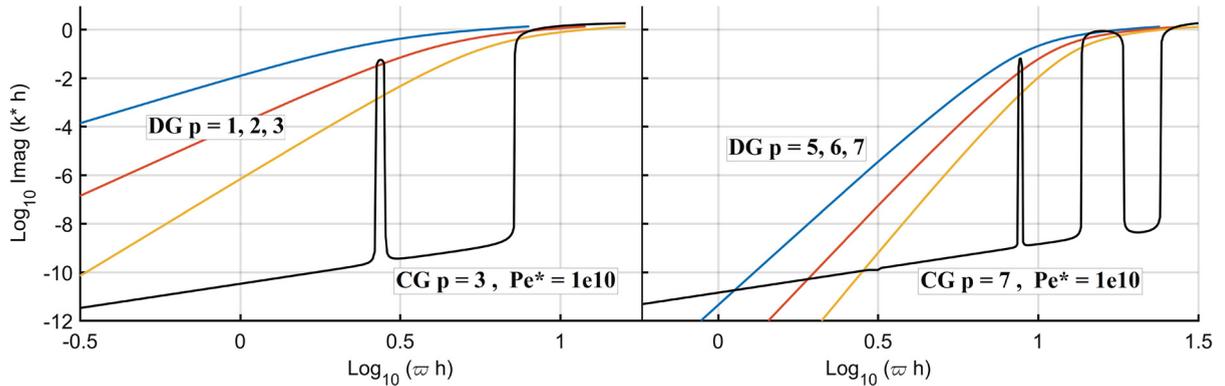
Fig. 7. Dissipation curves in log-log scale for CG-based advection-diffusion at Pe* $= 10^{10}$ with $P = 3$ (left) and $P = 7$ (right) compared against DG dissipation curves for P, $P - 1$ and $P - 2$ (colour).

The procedure adopted was to match the dissipation curves of CG with SVV stabilization of order P to those of DG of order $P - 2$. This was not only achievable through the optimisation procedure, but also addressed the issue of CG's dissipative bubbles. The latter were naturally covered by the dissipation levels typical of DG at order $P - 2$, as can be anticipated from Fig. 7. The kernel entries obtained from the optimisation process for different polynomial orders are given below. The corresponding optimised dissipation curves are shown in Fig. 8. Note that focus is given to higher-order discretizations ($P > 2$), which are the ones requiring more stabilization.

- $P = 3 : 0, 0.70546, 0.078836, 1$
- $P = 4 : 0, 0, 0.49411, 0.072394, 1$
- $P = 5 : 0, 0, 0.0000735, 0.40506, 0.094122, 1$
- $P = 6 : 0, 0, 0, 0.0001422, 0.36863, 0.11815, 1$
- $P = 7 : 0, 0, 0, 0, 0.00019497, 0.41397, 0.16927, 1$
- $P = 8 : 0, 0, 0, 0, 0, 0.0009762, 0.12747, 0.13763, 1$
- $P = 9 : 0, 0, 0, 0, 0, 0, 0.0023592, 0.23683, 0.17196, 1$
- $P = 10 : 0, 0, 0, 0, 0, 0, 0, 0.0026055, 0.28682, 0.22473, 1$

A first point deserving some comments is the non-monotonic behaviour of the kernel entries above, as intuitively one might expect this to lead to non-monotonic dissipation curves. Although it is not clear at this point why this is not the case here, a possible explanation is that SVV needs only to provide a dissipation distribution to fill the gap between the (monotonic) DG curve of order $P - 2$ and that of inviscid CG of order P, which features (non-monotonic) bubbles. Another important point is that matching was performed mostly for the regions of constant slope in log-log plots, as will be described below. This caused the dissipation levels that are more evident in linear scale plots (cf. right-hand side of Fig. 8) to be basically a by-product of the optimisation process. However, the matching at higher frequencies does not need to be perfect, and the fact the CG dissipation levels in this range were typically stronger than expected is actually good for robustness.

The optimisation procedure conducted consisted essentially in minimizing the distance between a reference DG curve and that yielded by a trial SVV kernel at a set of equispaced points along the DG curve. Their position covered mostly the region of constant slope (in log-log plots) for each DG curve. The number of points was chosen to be twice the number of free kernel entries for each case. Note that the first entry is always zero for a proper SVV operator, whereas the last one is a (unit) dummy entry that actually does not affect the eigencurves [15]. Hence, the CG discretization with $P = 3$, for example, had only two free kernel entries to be adjusted. Optimisation was performed via MATLAB's global optimisation toolbox. Different algorithms have been tested, but the best results were achieved with the so-called Particle Swarm approach, see e.g. [32], through MATLAB's function *particleswarm*. This is a nongradient-based algorithm that optimizes a problem by iteratively trying to improve a candidate solution with regards to a given objective function. A population of candidate solutions, called particles, moves around in search-space towards the best solution under the influence of the whole population. By analogy one might think of a swarm of birds seeking a source of food. In this scenario, each bird/particle relies on its own

perception as well as on the knowledge gained by the swarm as a whole in order to find the best source of food. A recent review on the subject can be found in [33].
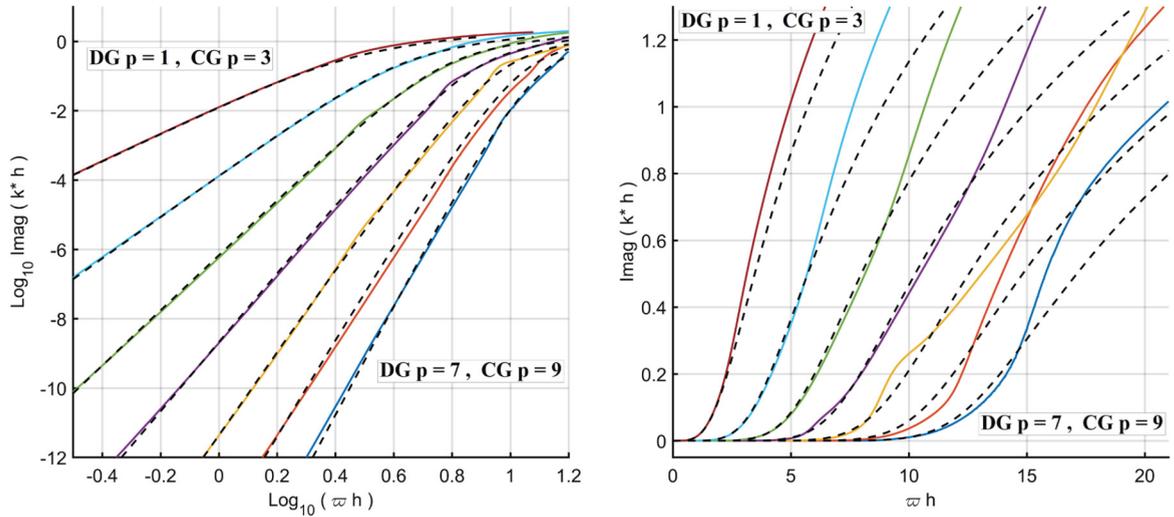
Fig. 8. Comparison between optimised CG-SVV dissipation (colour) for $P_{CG} = 3, \ldots, 9$ and their reference DG curves (dashed) for $P_{DG} = 1, \ldots, 7$. The polynomial order of the curves increases from left to right in both the log-log (left) and linear scale (right) plot.
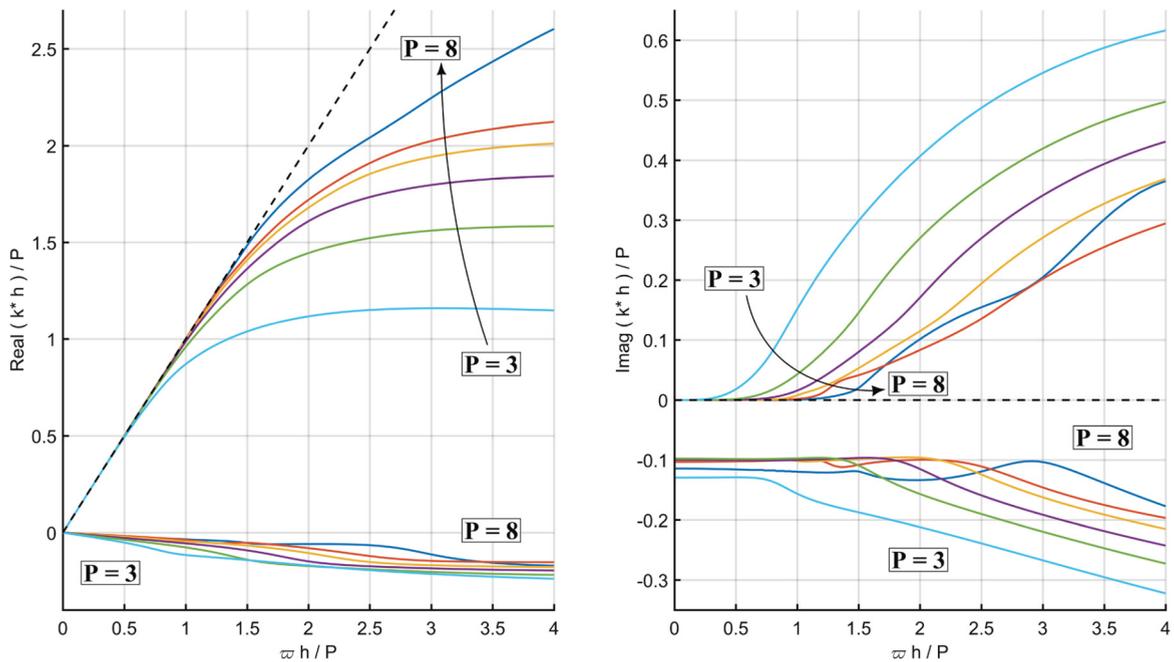
Fig. 9. Numerical dispersion (left) and diffusion (right) characteristics of the CG-SVV approach proposed for $P = 3, \ldots, 8$. Such DOF-based plots indicate superior resolution power per DOF at higher polynomial orders (arrows). Physical (top) and spurious (bottom) eigenmodes are shown.

At this point, it is worth explaining why the unit Péclet number ($Pe^* = \mu_0^{-1} = 1$) was chosen for the SVV operators considered in this study. We note that the SVV characteristics are actually defined by the product between μ_0 and the kernel entries. However, the optimal entries found were observed to be inversely proportional to whichever value of μ_0 was set for the optimisation. For example, when optimisations were performed with $\mu_0 = 10$, the optimal kernel entries obtained were exactly ten times smaller than the ones tabulated previously, resulting in the same dissipation curves. Hence, the reference Péclet value adopted for the SVV is not important in itself, and the unit value has only been chosen for convenience.

The optimised SVV operators were found to improve discretization robustness significantly, as will be discussed in Sec. 5. The accuracy at moderate orders was however not so good due to the fact that DG dissipation curves of order $P - 2$ were

used as reference. For example, CG at $P = 3$ had the dissipation levels of DG order $P = 1$, which are known to be too large e.g. for under-resolved turbulence computations [9,34]. Nevertheless, at higher polynomial orders, much smaller dissipation levels are achieved and the CG-SVV approach proposed becomes suitable for high-fidelity simulations. It should be stressed that, for well-resolved computations (e.g. laminar flows), CG's standard nominal order of accuracy of $P + 1$ is maintained. This is because, even though we match DG's dissipation at order $P - 2$, the resulting CG diffusion error still superconverges as $\Im(\kappa^* h) \propto (\varpi h)^{2(P-2)+2}$. Therefore, given sufficient resolution ($\varpi h \ll 1$) and assuming that diffusion error dominates, mesh refinement yields an algebraic decay slope of $2P - 2$, which is larger than $P + 1$ provided that $P > 2$.

Finally, the dispersion/diffusion eigencurves obtained with the optimised SVV operators are shown in Fig. 9 with the usual DOF-based plots. These confirm that a superior resolution power (based on the extent of the frequency range of negligible error) is achieved on a per DOF basis as the polynomial order is increased, for both dispersion and diffusion. An additional condition adopted in the optimisation process was the penalization of eigencurves whose dissipation values of the spurious mode were too small. More specifically, a requirement of $\Im(\kappa^* \hbar) < -0.1$ was set for the spurious modes. This of course made more difficult the attainment of low dissipation levels for the physical modes. The threshold of -0.1 was considered sufficiently strong to damp reflected waves over a short distance, based on the experiments conducted in connection with Fig. 3. The optimised DG-based SVV is tested in the next section.

5. Numerical experiments in under-resolved vortical flows

This section is devoted to the simulation of spatially developing vortex-dominated flows as a means to assess the fidelity and robustness of high-order CG discretisations with and without SVV. This is a preliminary step towards the assessment of CG-based simulations of more complex transitional/turbulent flows and should provide some insight into the scheme's behaviour for under-resolved computations. A model problem is considered that mimics to a certain degree a grid turbulence flow evolving inside a duct in a two-dimensional setting. This test case was originally proposed for DG in [16] and consists of a rectangular domain with inflow/outflow boundary conditions on the sides and free-slip wall conditions on the top and bottom boundaries. All simulations have been conducted with the incompressible Navier-Stokes solver of spectral/*hp* element code *Nektar++* [35].

The adopted model problem relies on inlet boundary conditions that mimic a passive generator of eddies (physical screen). This produces large-scale vorticity that propagates into and along the domain. Inflow conditions for the streamwise and cross-flow velocity components and for the pressure are set respectively as $u = 1 + 0.5 \sin(5y) \sin(t)$, $v = 0$ and $\partial p / \partial x = 0$, where x and y denote the Cartesian coordinates in the streamwise and cross-flow directions and t stands for the time. The domain top and bottom boundaries are situated at $y = \pm \pi$ and are assigned the conditions $\partial u / \partial y = 0$, $v = 0$ and $\partial p / \partial y = 0$. Finally, the outlet is placed 20π length units apart from the inlet and is subjected to the conditions $\partial u / \partial x = 0$, $\partial v / \partial x = 0$ and $p = 0$. All the results shown here correspond to solutions obtained after a temporal span of $\Delta t = 100$ time units, allowing for the (unit) mean velocity of the flow to sweep the streamwise extension of the domain approximately 1.5 times.

The SVV implementation adopted the optimised kernel entries discussed in Sec. 4, although the reference Péclet number was kept only approximately constant as the streamwise velocity was assumed to be the same (and equal to its unit mean value) throughout the flow. More specifically, SVV's base magnitude was set to $\mu_{SVV} = h/P$, where h is the local grid spacing in the streamwise direction. This was done to avoid a non-linear SVV operator of more complex implementation in this initial stage of testing. The base set of test cases consisted of uniform (equispaced) meshes of square-shaped elements, although cases of variable grid spacing have also been considered, as discussed further below. Test cases of polynomial order P with N elements in the cross-flow direction (hence 10 N elements in the streamwise direction) are denoted as "pPnN". The Reynolds number of the test cases was defined based on the (unit) flow mean velocity, the length scale $\pi/5$ representing the size of the inlet eddies, and the fluid's viscosity. The latter is varied to control the Reynolds number in the simulations.

All the test cases conducted without SVV lacked numerical stability and "crashed" as the Reynolds number was increased. In contrast, when SVV was introduced, all test cases became stable regardless of the Reynolds number (tests were conducted up to $Re = 10^8$). This is not surprising given the robust dissipation characteristics of DG reproduced by the optimised SVV operators. Obviously, for each given case, the solution at sufficiently high Reynolds "saturates" and remains practically unchanged as the fluid's viscosity is further decreased. This is because SVV dissipation effects eventually become more significant than those of molecular viscosity. This scenario resembles that of e.g. under-resolved DG computations in the limit of vanishing viscosity, where upwind dissipation remains alone to provide small-scale regularization [9,36,16]. In case of saturation, higher fidelity results will require an increased number of elements or a higher polynomial order. It should be stressed that, for a given number of DOFs, discretisations of higher order (and fewer elements) are to be preferred. This has been confirmed for a set of test cases with (approximately) the same number of DOFs for $P = 3, \ldots, 8$, as shown in Fig. 10. These cases are conducted at a Reynolds number of $Re = 1.5 \times 10^4$ and are nearly saturated considering the reduced number of DOFs employed. Increased resolution power is clearly achieved with higher orders thanks to the optimised SVV operators, cf. Fig. 9. It should be stressed that, without SVV, higher-order cases crashed at Reynolds numbers as low as 1500 due to instabilities developed around the "transitional" flow region near the inlet. Similar instabilities occurred for the lower order cases, although those took longer distances to form inside the domain. Case p3n28, for example, crashed slightly after $Re = 5000$.
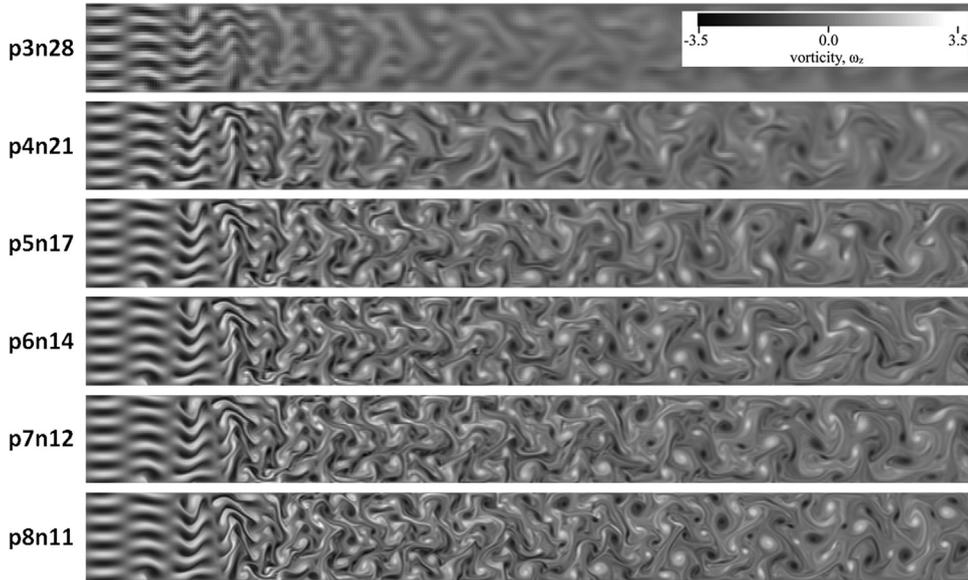
Fig. 10. Vorticity contours of same-DOF test cases for uniform (equispaced) meshes with various polynomial orders ($P = 3, \ldots, 8$) at $\mathrm{Re} = 1.5 \times 10^4$. Increased resolution is achieved with higher orders.
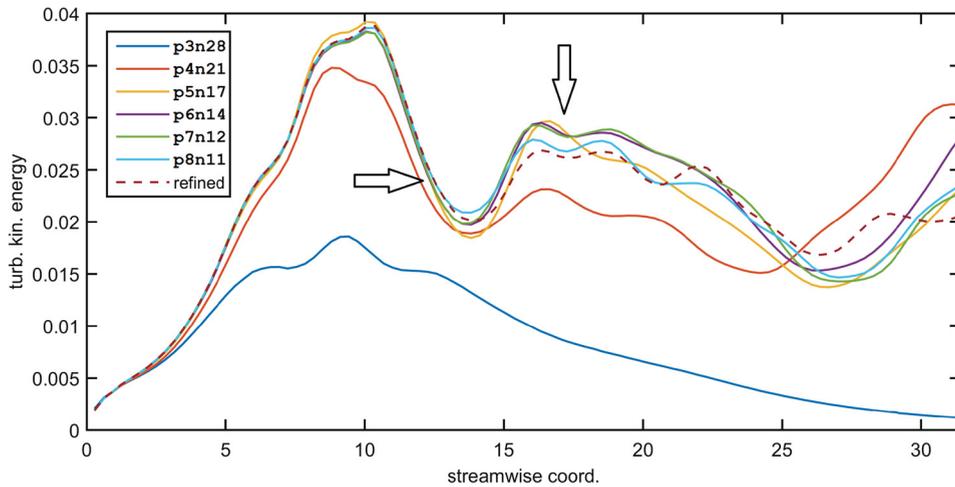
Fig. 11. Evolution of turbulent kinetic energy along the horizontal axis at mid-height ($y = 0$), for the cases shown in Fig. 10. The reference (dashed) curve has been obtained with $P = 8$, but with the finer mesh originally used for $P = 3$. The arrows indicate relevant regions of deviation for higher order cases.

In order to have a more quantitative measure of solution quality, the evolution of turbulent kinetic energy $\langle u^2 + v^2 \rangle/2$ along the horizontal axis at mid-height ($y = 0$) has been measured and is given in Fig. 11. Only the first (upstream) half of the domain is shown. These results have been time-averaged over $\Delta t = 50$ and then $\Delta t = 100$ time units after the asymptotic solution of Fig. 10 had been reached, with the curves remaining practically unchanged. In two-dimensional turbulence, the so-called inverse energy cascade plays a fundamental role through vortex merging at small scales via viscous effects [37]. This is believed to be causing the intermittent growth of turbulent kinetic energy along the domain seen in Fig. 11, contrary to the simple decay that would be expected in three-dimensional grid turbulence. The reference result (dashed curve in the plot) has been obtained with $P = 8$, but with the finest mesh available, i.e. the same used for case p3n28.

The first observation one can make from Fig. 11 is that case p3n28 is too dissipative to allow for small-scale vorticity to form, whereby its peak of kinetic energy is followed by a monotonic decay of large scales. Case p4n21, consistent with Fig. 10, already features the formation of small scales leading to subsequent intermittent growth of kinetic energy, but the reference peak energy is not well matched in value or position. Case p5n17 matches the peak energy in position, but slightly overestimates its value. Cases p6n14 and p7n12 are practically indistinguishable until later stages and reproduce well the whole region near the peak energy, although slightly underestimating its value. These two cases start to deviate more noticeably from the reference result at the region pointed by the first (left) arrow in the plot. Finally, case p8n11 takes

longer to deviate from the reference curve while also following it more closely along the next two peaks (second arrow in the plot). As the error accumulates nonlinearly along subsequent stages, case p8n11 is not necessarily the closest to the reference at all future stations. This type of comparison clearly illustrates how solution quality is recovered at higher orders for spatially developing problems.

Test cases conducted with mesh coarsening beyond a certain station of the domain have also been considered. In these cases, spurious reflections tend to originate from the interface where mesh spacing changes, affecting solution quality and potentially undermining numerical robustness. Nevertheless, it was difficult to relate the observed instabilities specifically to spurious reflections because the test cases without SVV are already unstable at relatively low Reynolds numbers, when the damping of spurious modes is not negligible. Note that, for cases without SVV, the (mean) Péclet value for uniform mesh regions (square-shaped elements) can be expressed as $Pe^* = Re/P$.

Vorticity contours of case p8n11 at $Re = 1000$ with and without SVV are shown in Fig. 12 when mesh coarsening is applied after the first 60% of the domain. For this case, streamwise spacing becomes four times larger for the domain's second block, whereas cross-flow spacing remains unchanged. Without SVV, reflections are very mild due to the low Reynolds number and can hardly be noticed even in vorticity contours, which rely on velocity gradients and hence tend to highlight numerical oscillations. Still, a closer look reveals the positive effects of SVV in suppressing spurious reflections without significantly affecting solution quality. Note that case p8n11 is unstable without SVV beyond the considered Reynolds number.
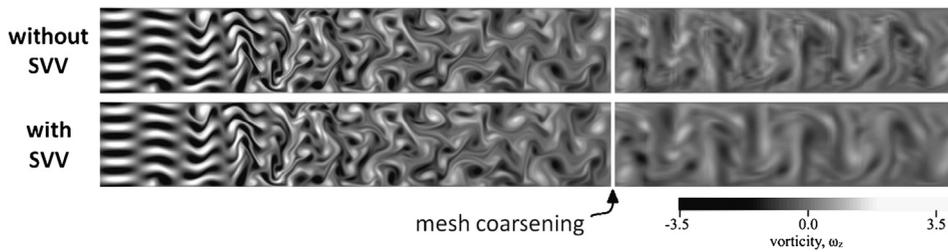
Fig. 12. Vorticity contours of case p8n11 at $Re = 1000$ with and without SVV when a four times larger streamwise spacing is used after the first 60% of the domain. Closer examination reveals that SVV is able to suppress spurious reflections from the interface of mesh spacing discontinuity.
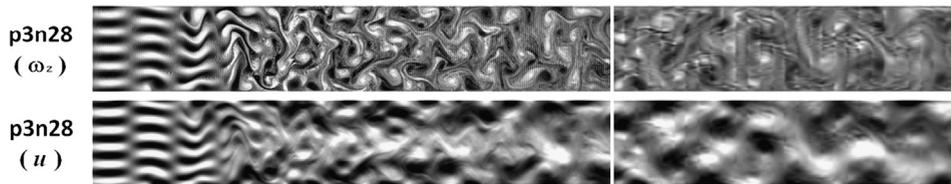
Fig. 13. Contours of vorticity and streamwise velocity for case p3n28 at $Re = 5000$ without SVV. Mesh coarsening is applied after station 60%. Isocontour levels are the same of Fig. 12, except that for the velocity contours its values range from 0.5 (black) to 1.5 (white).

Case p3n28 is stable without SVV at a higher Reynolds and has also been considered with the same type of mesh coarsening mentioned above to demonstrate how reflections become more prominent as molecular viscosity is further reduced. Contours of vorticity and streamwise velocity for case p3n28 at $Re = 5000$ (without SVV) are given in Fig. 13. These clearly highlight the adverse effects of spurious reflections on solution quality at higher Reynolds numbers. Adding SVV does suppress reflections, but also damps most of the relevant flow scales due to the lower order in question, as can be anticipated from Fig. 10 (upper plot). The sensible approach to high-fidelity under-resolved computations at high Reynolds is therefore to employ higher polynomial orders along with moderately coarse grids, so as to avoid spurious waves while retaining a superior resolution power. Still, in the next section, we show how SVV can be adjusted at lower polynomial orders in order to grant better results.

6. Lower orders and alternative kernels

In order to compare the optimised (DG-based kernel) SVV strategy with alternative ones, the spatial eigencurves given by the so-called power kernel proposed in [15] are shown in Fig. 14 (continuous curves). Note that only its temporal eigencurves had been considered in the literature so far owing to the focus of [15]. Compared to traditional kernels, such as the exponential kernel [38], the power kernel exhibits superior properties like a consistent increase in resolution power at higher orders in a same-DOF setting, as also discussed in [15]. Its kernel entries for element-wise modes $0 \leq j \leq P$ are given by

$$\hat{\mathcal{Q}}_j = (j/P)^{P_{SVV}} , \qquad (16)$$

where we adopt $P_{SVV} = P/2$ along with $Pe^* = a\hbar/\mu_{SVV} = 2$, as prescribed in [15].

From Fig. 14, the power kernel is clearly less dissipative for $P = 3$ than the proposed DG-kernel at the same order (blue top-most curves in the plot). In fact, the dissipation levels of the power kernel for $P = 3$ are between those of the DG-kernel for $P = 3$ and $P = 4$. Moreover, its associated spurious reflected mode (not shown) is strongly dissipated, namely $\Im(\kappa^*\hbar) < -0.6$. Therefore, the power kernel is to be preferred over the DG-kernel for $P = 3$. We note from Fig. 14 that, at this order, the superconvergent slopes are the same for both kernels. However, while this slope is maintained with the power kernel at higher orders, the DG-kernel achieves much steeper slopes (and hence much smaller dissipation levels) as P increases. This is clear already for $P = 4$ since the red dashed curve remains under the continuous red one for the whole superconvergent region. For $P \geq 5$, the superiority of the DG-kernel is even more clear, as one might anticipate from the large gap between the two bottom-most curves in the plot (representing $P = 9$). Also, we stress that it is nearly impossible to reduce even further the dissipation of the power kernel for $P = 3$ without having a non-monotonic curve. This has been found upon experimentation by changing the power kernel parameters P_{SVV} and Pe^*. Such limitation has to do with CG's dissipation bubble for $P = 3$ (cf. Fig. 7, left plot), to which the power kernel dissipation curve is nearly tangent.
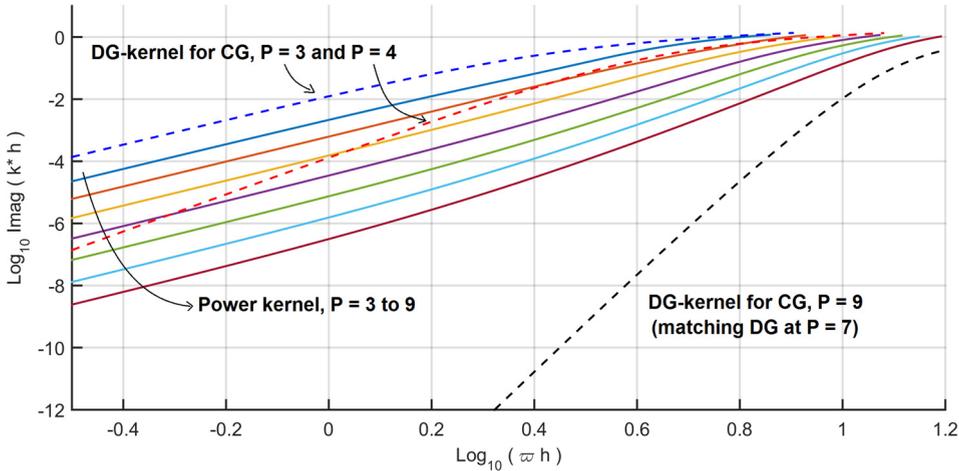
Fig. 14. Comparison between optimised CG-SVV dissipation (dashed) for $P_{CG} = 3, 4$ and 9, and the power kernel (continuous curves) from [15] for $P_{CG} = 3, \ldots, 9$. For both sets of curves, the polynomial order grows from top to bottom. The dashed curves are the same of Fig. 8 (left graph).

Finally, we consider case $P = 2$, which is the lowest order for which SVV can be used, having in this case only one free tunable parameter. As explained in Sec. 4, the first and last coefficients of the SVV kernel are dummy entries, whereby SVV's dissipation curve for $P = 2$ is entirely defined by the product between $\hat{\mathcal{Q}}_{j=1}$ and $\mu_0 = 1/Pe^*$. As the latter is set to one for convenience in the DG-kernel strategy, we only need to analyse the variation of $\hat{\mathcal{Q}}_{j=1}$. In this case, by changing this single kernel entry, all possible SVV operators for $P = 2$ are covered. At this order, we do not aim at matching DG's dissipation. The variation of all possible curves is somewhat involved and is illustrated with a pair of plots in Fig. 15. Noting that $\hat{\mathcal{Q}}_{j=1} \leq 1$, we first decrease its value from 0.9 to 0.1 in the upper plot, where one sees the dissipation decreasing at intermediate frequencies while increasing at lower ones. Surprisingly, because of this, the superconvergent slope gradually becomes less steep, moving away from that of the DG-kernel at $P = 4$ (red dashed curve) towards that of the DG-kernel at $P = 3$ (blue dashed curve), which however is only attained at smaller values of $\hat{\mathcal{Q}}_{j=1}$. The dissipation curve for the power kernel at $P = 3$ is shown as well for reference (black dotted curve). In addition we note that the power kernel at $P = 2$ is recovered for $\hat{\mathcal{Q}}_{j=1} = 0.5$, appearing as a yellow curve in the upper plot.

Moving to the lower plot in Fig. 15, we first decrease $\hat{\mathcal{Q}}_{j=1}$ from 0.1 to 0.01 (top-most curves' set) and then from 10^{-3} to 10^{-6} (bottom-most curves' set). It is clear that after $\hat{\mathcal{Q}}_{j=1} \approx 0.035$, decreasing further its value only reduces SVV's overall dissipation while keeping the superconvergent slope fixed as that of the DG-kernel at $P = 3$. We also note that when $\hat{\mathcal{Q}}_{j=1} < 0.035$, the dissipation of the spurious reflected mode (not shown) becomes too weak, namely $\Im(\kappa^*\hbar) > -0.1$, violating the criterion followed in the DG-kernel strategy, cf. Fig. 9 (right plot). In summary, we advise users to experiment with kernel entry values within $0.3 \leq \hat{\mathcal{Q}}_{j=1} \leq 0.06$. Higher values will result in dissipation levels stronger than those of the DG-kernel for $P = 3$ (at intermediate/small scales), whereas lower values lead to weak dissipation of spurious eigenmodes. We stress in particular that when $\hat{\mathcal{Q}}_{j=1} \approx 0.065$, SVV's dissipation for $P = 2$ matches that of the power kernel for $P = 3$ (black dotted curve) for a significant range of frequencies, while remaining under it in the superconvergent region. This is very significant because the considered plots compare dissipation curves under same-mesh (not same-DOF) settings. Hence, one can favour this specific kernel with $P = 2$ over a $P = 3$ discretisation with the power kernel, the latter being our best option for $P = 3$ so far. This fortuitous fact is only possible because discretisation $P = 2$ features no dissipation bubble — apart from that observed on the right-hand side of the lower plot in Fig. 15, which only appears at large frequencies (small scales).
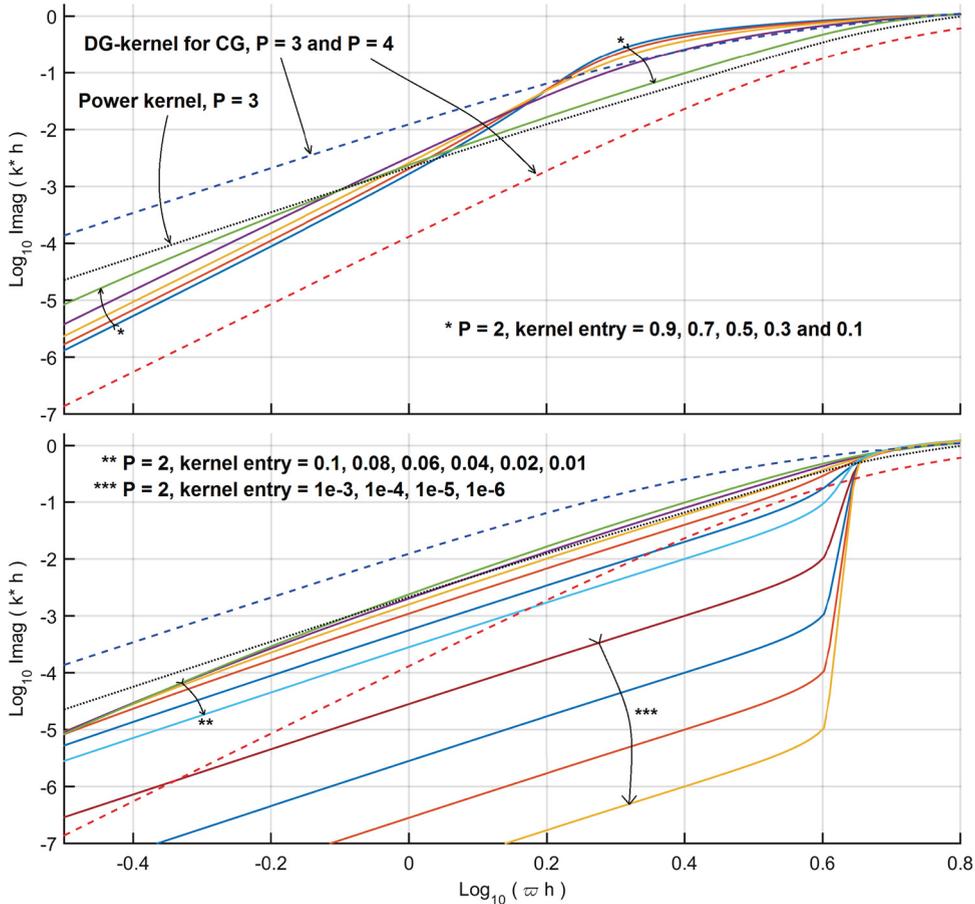
Fig. 15. SVV's dissipation for $P_{CG} = 2$ and different values of $\hat{\mathcal{Q}}_{j=1}$ (continuous curves), first from 0.9 to 0.1 (top plot, $\star$), then 0.1 to 0.01 (bottom plot, $\star\star$) and finally 10^{-3} to 10^{-6} (bottom plot, $\star\star\star$). Arrows with stars show the direction of decreasing $\hat{\mathcal{Q}}_{j=1}$. For reference, the DG-kernel dissipation is shown for $P_{CG} = 3$ (blue dashed curve) and $P_{CG} = 4$ (red dashed curve); the dissipation of the power kernel is also shown for $P_{CG} = 3$ (black dotted curve).

7. Conclusion

We have addressed the spatial eigenanalysis of spectral/*hp* continuous Galerkin (CG) methods as applied to the linear advection-diffusion equation and to the advection equation with added spectral vanishing viscosity (SVV). The work was motivated by two previous studies, namely, one that considered CG's temporal eigenanalysis [15] and another that addressed the spatial analysis of DG schemes [16]. Here, the influence of viscous effects have been assessed through the variation of the so-called Péclet number, which can be regarded as a numerical Reynolds number based on the local mesh size. A spurious wave mode associated to unphysical reflections was found to exist no matter the Péclet number. The stabilization of CG at large Péclet numbers was also discussed, and a novel SVV strategy was proposed for spatially developing flows. This strategy was tested on a two-dimensional vortex-dominated model problem designed to approximate the behaviour of a grid turbulence flow. The test cases addressed supported the excellent potential of the proposed approach, especially at higher polynomial orders, for under-resolved computations of transitional and turbulent flows.

In the spatial eigenanalysis, the inviscid (large Péclet) limit received particular attention due to residual dissipative effects with peculiar characteristics found to exist in this limit. More specifically, "dissipation bubbles" were observed for certain frequency ranges. Those might induce undesirable non-smooth diffusion features on CG-based under-resolved simulations of spatially developing flows at high Reynolds numbers. Moreover, the damping of spurious reflected waves was found to become negligible in the inviscid limit for a large range of frequencies. As these also have the potential to negatively affect solution quality, an SVV-based stabilization approach was sought that could suppress the adverse effects of dissipative bubbles and spurious reflections. This led to an optimisation strategy that matched SVV diffusion levels to those of (standard upwind) DG at a lower order. Given that DG dissipation curves were too steep (in log-log scale) owing to DG's super-convergent behaviour [31], the optimisation process employed was not able to match dissipation levels of same polynomial order. The achievable alternative was to match CG-SVV diffusion levels at order P to those of DG at order $P - 2$. This naturally solved the issue of dissipative bubbles as the optimised SVV diffusion levels were sufficient to overcome those of the bubbles, resulting in smooth dissipation curves for the proposed CG-SVV discretisation. Regarding the apparently large

gap between polynomial orders P and $P - 2$, we note that: (*i*) CG's standard order of accuracy for smooth problems is preserved at high orders ($P > 2$) since the optimised dissipation curves superconverge with slope $2P - 2$; and (*ii*) diffusion levels have been matched on a same-mesh basis (rather than same-DOF basis), in which case DG can only be expected to display higher accuracy because, at the same P, it has one additional independent DOF when compared to CG.

The optimised SVV operator was tested in a model problem mimicking grid turbulence, where CG's performance was analysed for spatially developing under-resolved vortical flows. While test cases without SVV lacked numerical stability even at low Reynolds numbers, those relying on SVV remained stable even in the limit of vanishing viscosity. Although lower order discretisations (e.g. third polynomial order) were found to be excessively diffusive, higher order results displayed excellent performance. In fact, increasing the order rapidly recovered the superior resolution capabilities of high-order DG [9,36,16], while at the same time suppressing unphysical features such as spurious reflections. At lower/moderate orders, specifically $P = 2$ and $P = 3$, alternative SVV kernels have been discussed and found to provide superior dissipation characteristics than those achieved by the DG-based strategy at these orders. Altogether, these techniques highlighted the strong numerical potential that appropriately stabilized spectral/*hp* CG methods have for high-fidelity simulations of transitional and turbulent flows at high Reynolds numbers.

Declaration of competing interest

The authors declare that they have no known competing financial interests or personal relationships that could have appeared to influence the work reported in this paper.

Acknowledgements

References

[1] J.A. Ekaterinaris, High-order accurate, low numerical diffusion methods for aerodynamics, Prog. Aerosp. Sci. 41 (3) (2005) 192–300.

[2] Z.J. Wang, High-order methods for the Euler and Navier-Stokes equations on unstructured grids, Prog. Aerosp. Sci. 43 (1) (2007) 1–41.

[3] S.K. Lele, Compact finite difference schemes with spectral-like resolution, J. Comput. Phys. 103 (1) (1992) 16–42.

[4] C. Bogey, C. Bailly, A family of low dispersive and low dissipative explicit schemes for flow and noise computations, J. Comput. Phys. 194 (1) (2004) 194–214.

[5] F.Q. Hu, M.Y. Hussaini, P. Rasetarinera, An analysis of the discontinuous Galerkin method for wave propagation problems, J. Comput. Phys. 151 (2) (1999) 921–946.

[6] K. Van den Abeele, T. Broeckhoven, C. Lacor, Dispersion and dissipation properties of the 1D spectral volume method and application to a p-multigrid algorithm, J. Comput. Phys. 224 (2) (2007) 616–636.

[7] K. Van den Abeele, C. Lacor, Z.J. Wang, On the stability and accuracy of the spectral difference method, J. Sci. Comput. 37 (2) (2008) 162–188.

[8] P.E. Vincent, P. Castonguay, A. Jameson, Insights from von Neumann analysis of high-order flux reconstruction schemes, J. Comput. Phys. 230 (22) (2011) 8134–8154.

[9] R.C. Moura, S.J. Sherwin, J. Peiró, Linear dispersion-diffusion analysis and its application to under-resolved turbulence simulations using discontinuous Galerkin spectral/*hp* methods, J. Comput. Phys. 298 (2015) 695–710.

[10] G. Mengaldo, D. De Grazia, R.C. Moura, S.J. Sherwin, Spatial eigensolution analysis of energy-stable flux reconstruction schemes and influence of the numerical flux on accuracy and robustness, J. Comput. Phys. 358 (2018) 1–20.

[11] P. Fernandez, R.C. Moura, G. Mengaldo, J. Peraire, Non-modal analysis of spectral element methods: towards accurate and robust large-eddy simulations, Comput. Methods Appl. Mech. Eng. 346 (2019) 43–62.

[12] G.E. Karniadakis, S.J. Sherwin, Spectral/hp Element Methods for Computational Fluid Dynamics, 2nd edition, Oxford University Press, 2005.

[13] E. Tadmor, Convergence of spectral methods for nonlinear conservation laws, SIAM J. Numer. Anal. 26 (1) (1989) 30–44.

[14] R.M. Kirby, S.J. Sherwin, Stabilisation of spectral/hp element methods through spectral vanishing viscosity: application to fluid mechanics modelling, Comput. Methods Appl. Mech. Eng. 195 (23) (2006) 3128–3144.

[15] R.C. Moura, S.J. Sherwin, J. Peiró, Eigensolution analysis of spectral/*hp* continuous Galerkin approximations to advection-diffusion problems: insights into spectral vanishing viscosity, J. Comput. Phys. 307 (2016) 401–422.

[16] G. Mengaldo, R.C. Moura, B. Giralda, J. Peiró, S.J. Sherwin, Spatial eigensolution analysis of discontinuous Galerkin schemes with practical insights for under-resolved computations and implicit LES, Comput. Fluids 169 (2018) 349–364.

[17] G.S. Karamanos, G.E. Karniadakis, A spectral vanishing viscosity method for large-eddy simulations, J. Comput. Phys. 163 (1) (2000) 22–50.

[18] R.M. Kirby, G.E. Karniadakis, Coarse resolution turbulence simulations with spectral vanishing viscosity–large-eddy simulations (SVV-LES), J. Fluids Eng. 124 (4) (2002) 886–891.

[19] R. Pasquetti, Spectral vanishing viscosity method for LES: sensitivity to the SVV control parameters, J. Turbul. 6 (12) (2005).

[20] M. Minguez, R. Pasquetti, E. Serre, High-order large-eddy simulation of flow over the 'Ahmed body' car model, Phys. Fluids 20 (9) (2008) 095101.

[21] J.-E.W. Lombard, D. Moxey, S.J. Sherwin, J.F.A. Hoessler, S. Dhandapani, M.J. Taylor, Implicit large–eddy simulation of a wingtip vortex, AIAA J. 54 (2) (2016) 506–518.

[22] R.C. Moura, S.J. Sherwin, J. Peiró, Modified equation analysis for the discontinuous Galerkin formulation, in: R.M. Kirby, M. Berzins, J.S. Hesthaven (Eds.), Spectral and High Order Methods for Partial Differential Equations - ICOSAHOM 2014, Springer, 2015, pp. 375–383.

[23] R.C. Moura, G. Mengaldo, J. Peiró, S.J. Sherwin, An LES setting for DG-based implicit LES with insights on dissipation and robustness, in: M. Bittencourt, N. Dumont, J.S. Hesthaven (Eds.), Spectral and High Order Methods for Partial Differential Equations - ICOSAHOM 2016, Springer, 2017, pp. 161–173.

[24] A.R. Winters, R.C. Moura, G. Mengaldo, G.J. Gassner, S. Walch, J. Peiró, S.J. Sherwin, A comparative study on polynomial dealiasing and split form discontinuous Galerkin schemes for under-resolved turbulence computations, J. Comput. Phys. 372 (2018) 1–21.

[25] R.C. Moura, J. Peiró, S.J. Sherwin, Implicit LES approaches via discontinuous Galerkin methods at very large Reynolds, in: M. Salvetti, V. Armenio, J. Fröhlich, B. Geurts, H. Kuerten (Eds.), Direct and Large-Eddy Simulation XI, Springer, 2019, pp. 53–59.

[26] H. Xu, C.D. Cantwell, C. Monteserin, C. Eskilsson, A.P. Engsig-Karup, S.J. Sherwin, Spectral/*hp* element methods: recent developments, applications, and perspectives, J. Hydrodyn. 30 (1) (2018) 1–22.

[27] J. Peiró, D. Moxey, M. Turner, G. Mengaldo, R.C. Moura, A. Jassim, M. Taylor, S.J. Sherwin, Spectral/*hp* element methods for under-resolved DNS: paving the way to industry-relevant simulations, ERCOFTAC Bull. 116 (2018) 5–13.

[28] J.D. Logan, V. Zlotnik, The convection-diffusion equation with periodic boundary conditions, Appl. Math. Lett. 8 (3) (1995) 55–61.

[29] M. Gaster, A note on the relation between temporally-increasing and spatially-increasing disturbances in hydrodynamic stability, J. Fluid Mech. 14 (02) (1962) 222–224.

[30] F.Q. Hu, H.L. Atkins, Eigensolution analysis of the discontinuous Galerkin method with nonuniform grids: I. One space dimension, J. Comput. Phys. 182 (2) (2002) 516–545.

[31] M. Ainsworth, Dispersive and dissipative behaviour of high order discontinuous Galerkin finite element methods, J. Comput. Phys. 198 (1) (2004) 106–130.

[32] G. Venter, J.S. Sobieski, Particle swarm optimization, AIAA J. 41 (8) (2003) 1583–1589.

[33] M.R. Bonyadi, Z. Michalewicz, Particle swarm optimization for single objective continuous space problems: a review, Evol. Comput. 25 (1) (2017) 1–54.

[34] G.J. Gassner, A.D. Beck, On the accuracy of high-order discretizations for underresolved turbulence simulations, Theor. Comput. Fluid Dyn. 27 (3–4) (2013) 221–237.

[35] C.D. Cantwell, D. Moxey, A. Comerford, A. Bolis, G. Rocco, G. Mengaldo, D. De Grazia, S. Yakovlev, J-E. Lombard, D. Ekelschot, B. Jordi, H. Xu, Y. Mohamied, C. Eskilsson, B. Nelson, P. Vos, C. Biotto, R.M. Kirby, S.J. Sherwin, Nektar++: an open-source spectral/*hp* element framework, Comput. Phys. Commun. 192 (2015) 205–219.

[36] R.C. Moura, G. Mengaldo, J. Peiró, S.J. Sherwin, On the eddy-resolving capability of high-order discontinuous Galerkin approaches to implicit LES / under-resolved DNS of Euler turbulence, J. Comput. Phys. 330 (2017) 615–623.

[37] G. Boffetta, R.E. Ecke, Two-dimensional turbulence, Annu. Rev. Fluid Mech. 44 (2012) 427–451.

[38] Y. Maday, S.M.O. Kaber, E. Tadmor, Legendre pseudospectral viscosity method for nonlinear conservation laws, SIAM J. Numer. Anal. 30 (2) (1993) 321–342.